ACS APPLIED MATERIALS & INTERFACES

www.acsami.org Research Article

Two-Step Chemical Vapor Deposition-Synthesized Lead-Free All-Inorganic $Cs_3Sb_2Br_9$ Perovskite Microplates for Optoelectronic Applications

Sujit Kumer Shil, Fei Wang, Kingsley O. Egbo, Zhengxun Lai, Ying Wang, Yunpeng Wang, Dongxu Zhao, Sai-Wing Tsang, Johnny C. Ho,* and Kin Man Yu*

Cite This: *ACS Appl. Mater. Interfaces* 2021, 13, 35930−35940 Read Online

ACCESS | Metrics & More | Article Recommendations | Supporting Information

ABSTRACT: Lead-based halide perovskites ($APbX_3$, where A = organic or inorganic cation, X = Cl, Br, I) are suitable materials for many optoelectronic devices due to their many attractive properties. However, the concern of lead toxicity and the poor ambient and operational stability of the organic cation group greatly limit their practical utilization. Therefore, there has recently been great interest in lead-free, environment-friendly all-inorganic halide perovskites (IHPs). Sb and Sn are common species suggested to replace Pb for Pb-free IHPs. However, the large difference in the melting points of the precursor materials (e.g., CsBr and $SbBr_3$ precursors for $Cs_3Sb_2Br_9$) makes the chemical vapor deposition (CVD) growth of high-quality Pb-free IHPs a very challenging task. In this work, we developed a two-step CVD method to overcome this challenge and successfully synthesized Pb-free $Cs_3Sb_2Br_9$ perovskite microplates. $Cs_3Sb_2Br_9$ microplates ~25 μm in size with the exciton absorption peak at ~2.8 eV and a band gap of ~2.85 eV were obtained. The microplates have a smooth hexagonal morphology and show a large Stokes shift of ~450 meV and exciton binding energy of ~200 meV. To demonstrate the applications of these microplates in optoelectronics, simple photoconductive devices were fabricated. These photodetectors exhibit a current on/off ratio of 2.36×10^2, a responsivity of 36.9 mA/W, and a detectivity of 1.0×10^{10} Jones with a fast response of rise and decay time of 61.5 and 24 ms, respectively, upon 450 nm photon irradiation. Finally, the $Cs_3Sb_2Br_9$ microplates also show good stability in ambient air without encapsulation. These results demonstrate that the 2-step CVD process is an effective approach to synthesize high-quality all-inorganic lead-free $Cs_3Sb_2Br_9$ perovskite microplates that have the potential for future high-performance optoelectronic device applications.

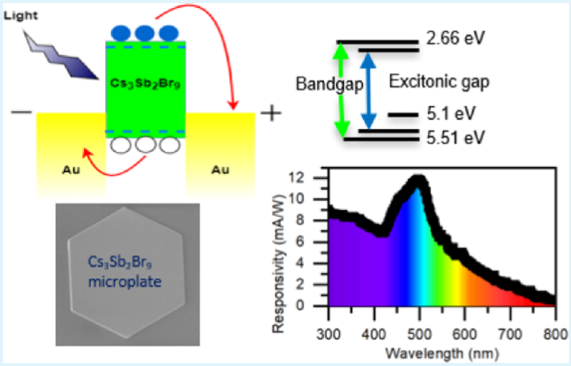

KEYWORDS: *all-inorganic, lead-free perovskite, $Cs_3Sb_2Br_9$, microplates, chemical vapor deposition, photodetector*

INTRODUCTION

In the last few years, organic hybrid halide perovskite materials ABX_3 (A = organic cation group, B = metal, X = halide) have attracted tremendous attention. Because of their intriguing optoelectronic properties, these materials can be widely used in many optoelectronic devices such as solar cells,[1−3] photodetectors,[4,5] light-emitting diodes,[6,7] and field-effect transistors.[8,9] In 2009, the first organic hybrid perovskite solar cell (PSC) was reported with a low efficiency of 3.5%.[1] However, after only a few years, the power conversion efficiency of PSCs has soared to over 25.2%, comparable to commercial crystalline silicon photovoltaics.[10]

Despite their tremendous recent success, devices fabricated from organic hybrid perovskites still suffer from long-term instability. This has been attributed to the sensitivity of the organic cation groups to oxygen, moisture, and environmental stress.[11−13] To alleviate this material instability, several different inorganic elements have been considered as replacements to the organic cation groups (e.g., Cs, Rb).[14,15] Accordingly, all-inorganic cesium lead halide perovskites ($CsPbX_3$, X = Cl, Br, I) have been studied and are also regarded as promising candidates in many optoelectronic applications including solar cells,[16−18] photodetectors,[19,20] lasers,[21,22] light-emitting diodes,[23,24] and photocatalytic CO_2 reduction[25,26] due to their distinctive properties, such as large absorption cross section, long diffusion length, high carrier mobility, long carrier lifetimes, and low trap densities.[27−31] Despite the remarkable advances achieved in $CsPbX_3$ perovskites, the high toxicity of Pb is a great obstacle for their

Received: May 3, 2021
Accepted: July 13, 2021
Published: July 21, 2021

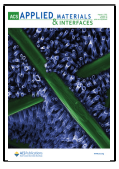

https://doi.org/10.1021/acsami.1c07839
ACS Appl. Mater. Interfaces 2021, 13, 35930−35940

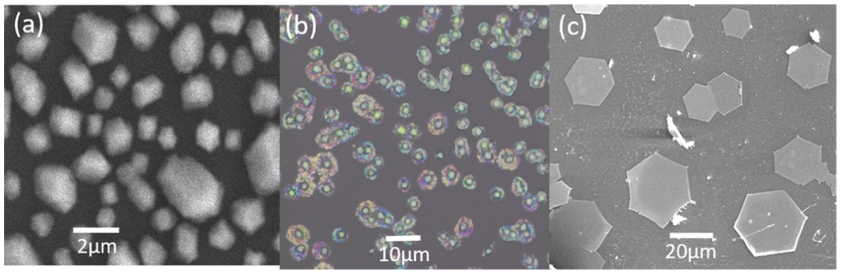

Figure 1. SEM micrographs showing the $Cs_3Sb_2Br_9$ microplates evolution. (a) SEM image after Step I growth. (b) Optical image of Step II. (c) SEM image of the microplates obtained after annealing.

widespread commercial applications. Therefore, much attention has been devoted to the search for Pb-free inorganic perovskites for optoelectronic device applications.[32,33]

The replacement of the Pb^{2+} ion with other metal ions in $CsPbX_3$ perovskites is challenging due to the limited availability of alternative metals that can satisfy the Goldschmidt tolerance factor for a close-packed perovskite structure.[34] In this respect, the substitution of a Pb^{2+} ion with divalent Sn^{2+} or Ge^{2+} is a possible choice. However, recent reports have shown that both Sn^{2+} and Ge^{2+} easily oxidize to their tetravalent state (Sn^{4+}, Ge^{4+}) in air and lose their outermost ns^2 electrons, thus resulting in dominant defects of halogen vacancies and metal interstitials (Sn or Ge).[33−36] Lately, stable $A_3M_2X_9$ structure defect-ordered perovskites have been proposed. In these $A_3M_2X_9$ perovskites, two-third of the B sites of the conventional ABX_3 are replaced by M (either Bi^{3+} or Sb^{3+} ions), while a portion of the metal sites are replaced by vacancies.[37−39] Heterovalent replacement of Pb^{2+} by Bi^{3+} in perovskite nanocrystals with large carrier effective masses has been reported.[39,40] Sb-based $Cs_3Sb_2I_9$ perovskite thin films were also synthesized, showing a nearly direct band gap with a high absorption coefficient ($>10^5$/cm) and small electron and hole effective masses.[41] Recently, a few studies on $Cs_3Sb_2Br_9$ perovskites with different morphologies, such as nanocrystals, quantum dots (QDs), and nanoflakes, were also reported.[42−45] For example, Lu et al. synthesized $Cs_3Sb_2Br_9$ perovskite nanocrystals (NCs) by the hot injection method and demonstrated a 10-fold increase in their performance for solar-driven CO_2 reduction reaction compared to $CsPbBr_3$ NCs, producing over 500 μmol CO g^{-1} catalyst over the course of 4 h.[42] Ma et al. synthesized $Cs_3Sb_2Br_9$ QDs using a modified supersaturated recrystallization method, which showed a bright violet emission with a high photoluminescence quantum yield (PLQY) of 51.2%.[44] An inverse temperature crystallization method was used by Zheng et al. to synthesize submillimeter-sized $Cs_3Sb_2Br_9$ nanoflakes, which exhibited outstanding photodetector performance, such as high responsivity (3.8 A/W) and detectivity (2.6×10^{12} Jones).[43] Liu et al. reported millimeter-sized $Cs_3Sb_2Br_9$ perovskite single crystals prepared by the solvothermal method and fabricated photodetectors showing a fast response speed (0.2/0.3 ms), high responsivity (2.29 A/W), and sharp detectivity (3.77×10^{12} Jones).[45]

To date, in most reports, Sb-based perovskites, in particular, $Cs_3Sb_2Br_9$ perovskites, were synthesized by solution processing, which has the unique advantages of being low-cost and facile. However, it also involves difficulty in making the reactions proportional and uniform due to the different solubilities of precursors in the solvents. Moreover, the materials synthesized by solution processes usually incorporate a high concentration of impurities from the precursors, solvents, or surfactants, and their crystalline quality is inferior to those grown by high-temperature physical or chemical vapor methods.[46] Compared to solution-processing growth, chemical vapor deposition (CVD) is a well-established method to synthesize high-quality and high-purity semiconductor materials that can achieve excellent optoelectronic properties. CVD has also been demonstrated to be especially suited for the growth of micro- and nanostructures with high surface-to-volume ratio, good crystalline quality, and low defect density. In fact, the CVD method offers several advantages over the solution method for material synthesis. First, in the CVD method, the precursor ratio and reaction rate can be easily controlled by the growth temperature and flow rate; therefore, it is a highly controllable and easily adjustable method. Second, the CVD method is a high-temperature growth process, and due to the high thermal energy, the deposited species have a high mobility on the substrate and are able to crystallize to form high-quality single crystals. Despite these advantages, no report on the successful synthesis of $Cs_3Sb_2Br_9$ perovskites using the CVD method is available so far. This may be attributed primarily to the extreme melting point disparity for the precursors used, namely CsBr (636 °C) and $SbBr_3$ (96 °C).

In this work, a two-step CVD approach is developed to grow $Cs_3Sb_2Br_9$ microplates to overcome the challenges encountered in a conventional CVD process. We note that the two-step CVD process described here is slightly different from previously reported two-step processes.[47] In this two-step CVD process, after the sequential deposition of binary compounds in step I and step II, a low-temperature annealing process is used to form the ternary microplates. Using this new CVD approach, we successfully synthesized all-inorganic and lead-free $Cs_3Sb_2Br_9$ microplates with a lateral dimension of ∼10−50 μm and a thickness of ∼100−400 nm. The CVD-grown $Cs_3Sb_2Br_9$ microplates have a hexagonal morphology and exhibit a Stokes shift as large as ∼450 meV and an exciton binding energy of ∼200 meV. We also use these $Cs_3Sb_2Br_9$ microplates to fabricate photoconductive devices that show a reasonable performance with an on/off current ratio reaching 2.36×10^2, responsivity of up to 36.9 mA/W, and detectivity of up to 1.0×10^{10} Jones at an irradiation wavelength of 450 nm. Moreover, relatively fast rise and decay times of 61.5 and 24 ms, respectively, are demonstrated. These results clearly suggest that the two-step CVD process can be used to synthesize high-quality all-inorganic and lead-free $Cs_3Sb_2Br_9$ perovskite microplates that are potentially useful for the fabrication of high-performance optoelectronic devices.

https://doi.org/10.1021/acsami.1c07839
ACS Appl. Mater. Interfaces 2021, 13, 35930−35940

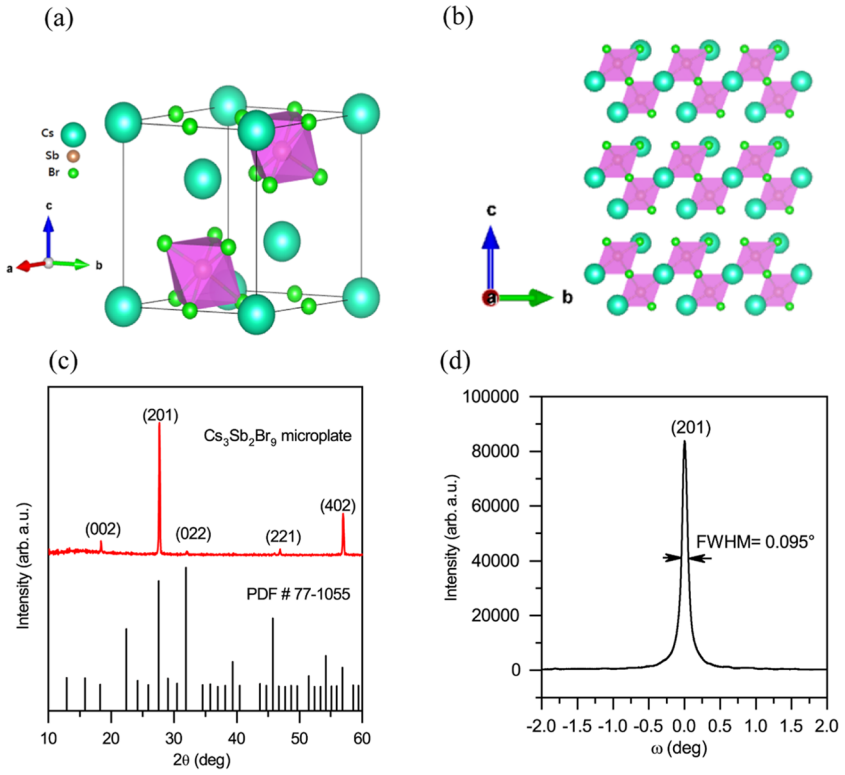

Figure 2. Structural characterization of $Cs_3Sb_2Br_9$ perovskite microplates. (a) Schematic representation of the atomic model of a $Cs_3Sb_2Br_9$ unit cell. (b) 2D layered $Cs_3Sb_2Br_9$ perovskite. (c) XRD patterns of the microplates. (d) Rocking curve for the (201) plane of $Cs_3Sb_2Br_9$ perovskite microplates.

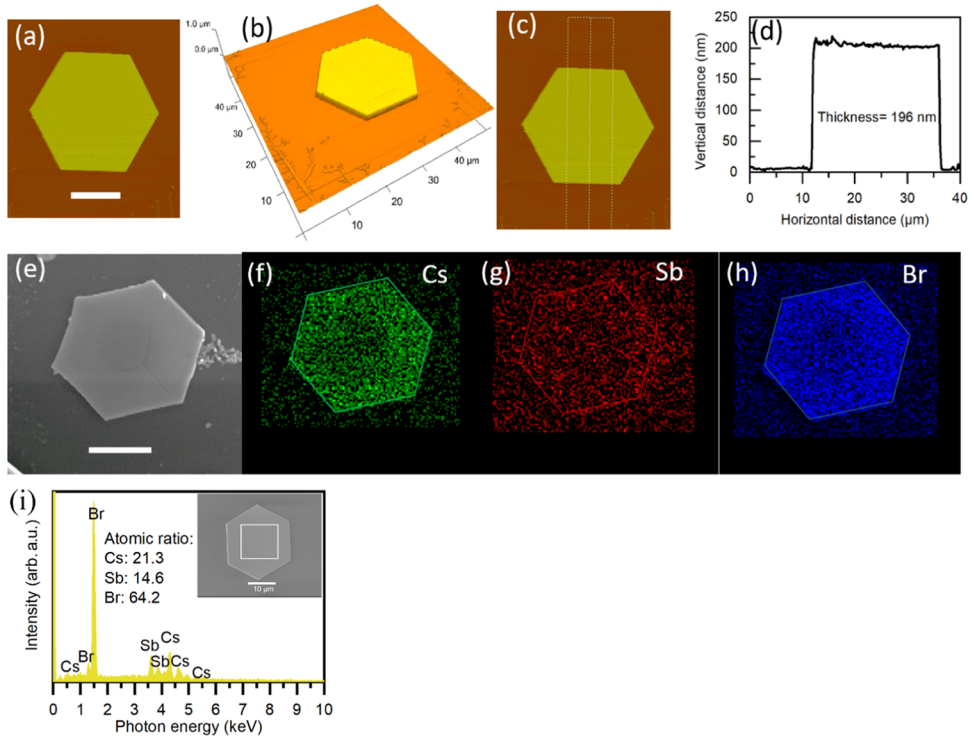

Figure 3. Morphology and composition analysis of $Cs_3Sb_2Br_9$ perovskite microplates. (a) AFM image of a single microplate. (b) 3D view of the corresponding microplate. (c) Line scan across the microplate showing the corresponding thickness in (d). (e) SEM image of an individual microplate. (f–h) EDX mapping of the corresponding microplate, showing the uniform distribution of different elements over the microplate. (i) EDX spectrum of a single microplate along with the corresponding elemental ratio. The scale bars in all images are 10 μm.

https://doi.org/10.1021/acsami.1c07839
ACS Appl. Mater. Interfaces 2021, 13, 35930−35940

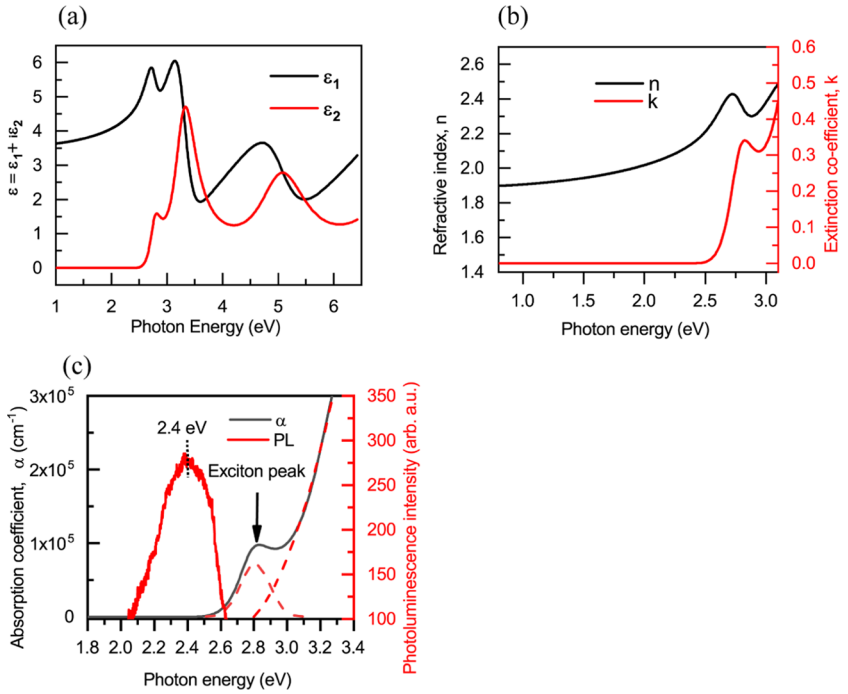

Figure 4. Optical characterization of $Cs_3Sb_2Br_9$ perovskite microplates. (a) Real and imaginary parts of the ε spectrum of a $Cs_3Sb_2Br_9$ perovskite microplate. (b) Optical constants of the $Cs_3Sb_2Br_9$ perovskite microplate. (c) Absorption coefficient along with steady-state photoluminescence spectra.

RESULTS AND DISCUSSION

Since the melting point of CsBr (636 °C) is much higher than that of the $SbBr_3$ precursor (96 °C), the chemical vapor growth of $Cs_3Sb_2Br_9$ perovskite by simply mixing the two precursors with the correct molar ratio and with the growth chamber heated to a high temperature resulted in the formation of CsBr on the substrate with the Sb preferentially vaporized and deposited on the tube surface. Here we developed a two-step CVD approach to achieve the growth of $Cs_3Sb_2Br_9$ perovskite microplate structures in a single-zone tube furnace as illustrated schematically in the Supporting Information (Figure S1). The CsBr precursor was first grown in step I in an optimized condition with the furnace temperature of 530 °C (Figure 1a). Then, the $SbBr_3$ precursor layer was grown over the CsBr-deposited substrates at a much lower temperature (90 °C) in step II (Figure 1b). In this step, $SbBr_3$ vapor followed the grown CsBr and deposited on the CsBr structures. The as-grown layers after the two-step CVD did not react completely as evidenced from the XRD patterns of individual growth shown in Figure S2. Complete reaction of CsBr and $SbBr_3$ occurs after annealing at 140 °C for 25 min. Since $SbBr_3$ has a very low melting point, it melts during annealing and gradually diffuses into the CsBr layer. After the recrystallization, the $Cs_3Sb_2Br_9$ perovskite microplates were formed on the substrate (Figure 1c). Note that the microplates formed have a hexagonal structure with a rough dimension of ~10−50 μm. Along with the diffusion, evaporation of $SbBr_3$ precursor also occurs during annealing. Therefore, to achieve the stoichiometric $Cs_3Sb_2Br_9$ perovskites, excess $SbBr_3$ source precursor was used. The elemental composition of the as-grown sample before annealing was analyzed by X-ray fluorescence spectroscopy (XRF) measurements and the corresponding spectrum is shown in Figure S3. The elemental ratio of Cs/Sb/Br is estimated to be 7.6:15.3:77.1. This confirms that while the Sb/Cs atomic ratio of stoichiometric $Cs_3Sb_2Br_9$ is 0.67, the as-grown layers are Sb-rich with an Sb/Cs ratio of ~2. Details of the growth processes are described in the Experimental Section. The optical images of the $Cs_3Sb_2Br_9$ microplates formed on different substrates (sapphire, glass, SiO_2-coated Si, and FTO-coated glass) obtained after annealing are presented in the Supporting Information (Figure S4).

The unit cell and 2D layered structure of $Cs_3Sb_2Br_9$ perovskite are drawn based on the crystallographic data[48] shown in Figure 2a,2b. Specifically, to achieve charge balance, 10 Cs cations surround the bi-octahedral $(Sb_2Br_9)^{3-}$ clusters in a $Cs_3Sb_2Br_9$ perovskite. The XRD pattern from the microplate sample shown in Figure 2b reveals that the diffraction peaks correspond to the 2D layered $Cs_3Sb_2Br_9$ perovskite structure (JCPDS No. 77-1055) with a preferred (201) alignment. The XRD measurement confirms that the perovskite microplates have a trigonal structure with lattice parameters of $a = b = 7.93$ Å, $c = 9.716$ Å, and angles of $\alpha = \beta = 90°$, $\gamma = 120°$, which are consistent with the space group of $P\bar{3}m1$ (164). Moreover, X-ray rocking-curve analysis around the (201) diffraction peak yields a very small peak width (FWHM) of 0.095° (or 342 arcsec) (Figure 2c), demonstrating that the microplates have high crystalline quality.

Atomic force microscopy (AFM) images and the line scan of typical $Cs_3Sb_2Br_9$ perovskite microplates are shown in Figures 3a−d and S5. The microplates show a well-defined hexagonal geometry with a lateral dimension of ~10−50 μm and a thickness of ~300 nm. The surfaces of the microplates are quite smooth with a surface roughness of ~1 nm. The elemental composition of these $Cs_3Sb_2Br_9$ microplates was analyzed using XRF and EDX measurements and show an atomic ratio (%) of Cs/Sb/Br = 21.7:12.9:65.4, in good agreement with the expected stoichiometric ratio (3:2:9) in $Cs_3Sb_2Br_9$ (Figure S6). The SEM image of a $Cs_3Sb_2Br_9$

https://doi.org/10.1021/acsami.1c07839
ACS Appl. Mater. Interfaces 2021, 13, 35930−35940

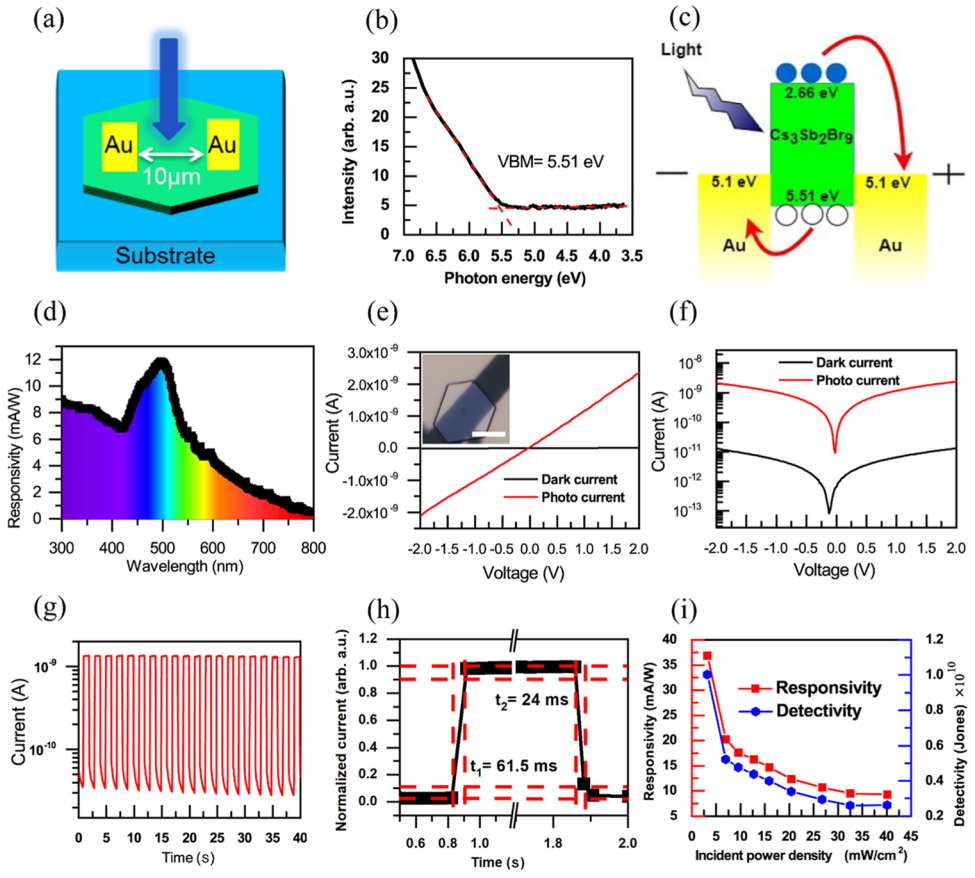

Figure 5. Photoconductive device characterization. (a) Schematic diagram showing the $Cs_3Sb_2Br_9$ microplate photodetector. (b) UPS spectrum of the $Cs_3Sb_2Br_9$ microplate showing its valence band maximum (VBM). (c) Schematic illustration of the alignment of energy bands and carrier transport in the photodetector under illumination. (d) Spectral response curve of the microplate photodetector. (e) Linear $I-V$ plot of the microplate photodetector under dark and 450 nm light illumination. An optical image of the device with a 10 μm scale bar is shown in the inset. (f) Logarithmic $I-V$ plot of the microplate photodetector under dark and 450 nm light illumination. (g) Multiple cycles of the device on/off switching under 47 mW/cm^2 incident power density. (h) Response of the device from the on/off switching characteristics. (i) Incident power-dependent responsivity and detectivity of the microplate photodetector under illumination with 450 nm photons.

microplate shown in Figure 3e and the corresponding elemental maps of Cs, Sb, and Br shown in Figure 3f–h illustrate the uniformity and homogeneity of the different constituents in the microplate. Figure 3i shows the EDX spectrum and corresponding elemental ratio of a single microplate (inset). Signals from different elements are clearly visible and the elemental ratio is very close to the $Cs_3Sb_2Br_9$ composition. The results from AFM and SEM confirm that these two-step CVD-grown perovskite microplates have high crystalline quality and crystal phase purity with close to 3:2:9 atomic ratio of $Cs_3Sb_2Br_9$. During recrystallization, along with the microplates, some three-dimensional (3D) structures also appeared. The EDX spectrum of a single 3D structure (Figure S7) confirmed that the composition is similar to that of $Cs_3Sb_2Br_9$ microplates.

The optical properties of $Cs_3Sb_2Br_9$ perovskite microplates were studied at room temperature by spectroscopic ellipsometry (SE). In the SE measurements, the incident beam was focused down to 300 μm, covering a cluster of microplates. The dielectric function ($\varepsilon = \varepsilon_1 + i\varepsilon_2$, where ε_1 and ε_2 are the real and imaginary parts of ε, respectively) of the $Cs_3Sb_2Br_9$ perovskite was derived by modelling the SE data by a series of Tauc–Lorentz (T–L) oscillators. Details of the modeling of the SE data are provided in the Supporting Information and Experimental Section. The dielectric function is related to the optical constants (refractive index n and extinction coefficient k) with the expressions $\varepsilon_1 = n^2 - k^2$ and $\varepsilon_2 = 2nk$. The absorption coefficient (α) is calculated from k using the relationship $\alpha = \frac{4\pi k}{\lambda}$. The real and imaginary parts of the dielectric functions ε_1 and ε_2 of the $Cs_3Sb_2Br_9$ microplates obtained from the SE analysis are shown in Figure 4a, while the optical constants are shown in Figure 4b. Figure 4b shows that the refractive index n of $Cs_3Sb_2Br_9$ is ~2.1 and the extinction coefficient is very low (close to 0) at the PL emission energy of 2.4 eV. Photoluminescence (PL) measurements were also carried out at room temperature to investigate the optical emission property of $Cs_3Sb_2Br_9$ perovskite microplates. The absorption coefficient obtained from SE measurement is plotted together with the PL emission peak in Figure 4c. Note that the absorption coefficient of $Cs_3Sb_2Br_9$ perovskite microplates is very high, ~1.5 × 10^5 cm^{-1} at ~3 eV. The absorption coefficient of the $Cs_3Sb_2Br_9$ microplates shows an absorption onset at ~2.65 eV and a discrete excitonic peak at ~2.8 eV, followed by an absorption continuum due to the band-to-band absorption. Deconvoluting the contribution due to the exciton absorption peak shows that the band-to-band absorption of the perovskite occurs at ~2.85 eV. This suggests that $Cs_3Sb_2Br_9$ has a large exciton binding energy of ~200 meV. This is much higher than the binding energies

https://doi.org/10.1021/acsami.1c07839
ACS Appl. Mater. Interfaces 2021, 13, 35930–35940

reported for Pb-based perovskites (24−32 meV for $MAPbI_3$ and 36−41 meV for $MAPbBr_3$)[49] and other semiconductor materials. This large exciton binding energy can be exploited using optoelectronic devices operating under high-temperature and intense irradiation conditions.

A broad and asymmetric PL peak with peak intensity at 2.4 eV is observed from the $Cs_3Sb_2Br_9$ microplates as shown in Figure 4c. A broad PL peak with similar peak energy was also reported by Zheng et al. for $Cs_3Sb_2Br_9$ nanoflakes synthesized by an inverse temperature crystallization method.[43] Compared to the absorption edge at 2.85 eV, the microplates exhibit a Stokes shift of ∼450 meV, which is much larger than the Stokes shifts in other semiconductor materials.[50,51] Note that for typical lead halide perovskites, Stokes shifts are on the order of ∼30−70 meV, which give rise to a strong self-absorption effect.[50,52] Note that a large Stoke shift (∼520 meV) was also found in our previous work of $Cs_3Sb_2I_9$ perovskite microplates.[53] The large Stokes shift of $Cs_3Sb_2Br_9$ perovskite microplates suggests that they are attractive candidates for light-emitting and laser diodes. However, a tail at a lower energy in the PL spectrum is also noticed, which may be due to the minor contribution of defect-related emissions from the $Cs_3Sb_2Br_9$ microplates. A similar long-wavelength tail in the PL spectrum was also reported in Sb-based halide perovskites grown by solution processes.[44,54]

The practical application of $Cs_3Sb_2Br_9$ microplates is further demonstrated by fabricating photoconductive devices with a metal/semiconductor/metal (MSM) configuration. The schematic diagram of a microplate photodetector is shown in Figure 5a. Before fabricating the device, we first determine the electronic band alignment with the metal. We determined the position of the valence band maximum (VBM) of $Cs_3Sb_2Br_9$ to be 5.51 eV below the vacuum level using ultraviolet photoelectron spectroscopy (UPS) (Figure 5b). The corresponding energy band alignment of the $Au/Cs_3Sb_2Br_9/Au$ structure is shown in Figure 5c. Here, Au has a work function of 5.1 eV and is considered a good contact metal for the MSM photodetector. Again, using Hall effect measurement, the Hall mobility of $Cs_3Sb_2Br_9$ material was obtained as ∼20 cm^2/Vs with a p-type conductivity of $\sim 3.4 \times 10^{-5}$ S/cm, and the carrier density was found to be $\sim 1.2 \times 10^{13}$ cm^{-3}.

The performance of photodetectors is normally characterized by their responsivity (R), which can be defined as

$$R = \frac{I_{ph}}{L_{light}} \tag{1}$$

where I_{ph} and L_{light} are the photocurrent and the incident light power, respectively. The spectral responsivity of the $Cs_3Sb_2Br_9$ microplate photodetector measured as a function of the irradiation wavelength is shown in Figure 5d. The device exhibits a maximum responsivity of 12 mA/W with incident photons of wavelength ∼500 nm. The responsivity then drops rapidly with increasing wavelength, and this behavior agrees with the absorption coefficient spectrum of $Cs_3Sb_2Br_9$ microplates as shown in Figure 4c. However, the absorption spectrum shows no absorption of photons with energy below 2.4 eV. This may be because the model used in analyzing the SE data may not be ideal and cannot capture the subgap absorption features. To clarify this discrepancy, the UV−vis spectrophotometry measurements were also performed, and the absorption spectrum is shown in Figure S10. Since the beam size is several mm and part of the incident beam passed through areas without microplate coverage, the absolute absorption cannot be obtained. Nevertheless, it is clear from Figure S10 that significant subgap absorption occurs at energies below 2.4 eV, which agrees with the responsivity results. Following the spectral responsivity, in the subsequent measurement of the device performance, an excitation light of wavelength 450 nm, closest to the maximum responsivity, was used.

Figure 5e (linear) and Figure 5f (log) show the current−voltage (I−V) characteristics of the microplate photodetector in the dark and under 450 nm light illumination with an incident power density of 40 mW/cm^2. An image of a typical device with an active area of $\sim 1.7 \times 10^{-6}$ cm^2 is shown in the inset of Figure 5e. The microplate photodetector exhibits a high resistance in the dark with a dark current of around 1.32×10^{-11} A at 2 V. When illuminated, the current increases to $\sim 2.36 \times 10^{-9}$ A. Note that the linear I−V curves indicate that the Au electrodes form good ohmic contacts with $Cs_3Sb_2Br_9$. The on/off photoswitching characteristics are also a key performance parameter for a photodetector. The successive on/off switching characteristics of the photodetector under 450 nm photon irradiation at 1 V bias shown in Figure 5g reveal no significant degradation over repeated switching cycles with an on/off current ratio of up to 2.36×10^2. Under 450 nm illumination, the rise (decay) time of the device, the time taken to increase (decrease) from 10 to 90% (90−10%) of its peak current, was determined to be 61.5 (24) ms, respectively (Figure 5h).

The dependence of the device photosensitivity on a range of illumination power densities was measured to study its performance stability under both weak and strong signals, and the results are shown in Figure S11. We observe increasing photocurrent when the power intensity increases from 3.2 to 40 mW/cm^2 under 450 nm light illumination, suggesting that more photocarriers are generated in the device with increasing incident photon intensity. The relationship between photocurrent (I) and the incident light power (P) was fitted by the power law $I = \beta P^{\alpha}$, where β is a proportionality constant and α is an exponential factor associated with its photoresponse corresponding to the light intensity. Figure S12 shows a fit of the power-dependent photocurrent of a microplate photodetector using this equation and yields a sublinear relationship of $\alpha = 0.49$, which results from the complex process of electron−hole generation, recombination, and trapping in the microplates.[55] The device responsivity plotted in Figure 5i as a function of the incident power shows that the highest value of 36.9 mA/W is achieved at a low incident power density of 3.2 mW/cm^2. The responsivity then drops rapidly to ∼9.5 mA/W and remains stable when the incident power density increases to a power intensity >30 mW/cm^2. The decrease in the responsivity may be related to the saturation of surface states and the filling of deep-level defects with the increased illumination power density.[56,57]

For an efficient photodetector with active area A, its detectivity (D^*), defined as the lowest level of light it can detect, is another important performance parameter and can be expressed in terms of the responsivity R and the dark current I_D as

$$D^* = \sqrt{\frac{A}{2qI_D}}R \tag{2}$$

https://doi.org/10.1021/acsami.1c07839
ACS Appl. Mater. Interfaces 2021, 13, 35930−35940

Table 1. Comparsion of the Key Performance Parameters of Reported Lead-Free All-Inorganic Perovskite Photodetectors

material	method/morphology	detecting wavelength (nm)	responsivity (mA/W)	detectivity (Jones)	rise/decay time (ms)	references
$Cs_3Bi_2I_9$	solution/single crystal	462	1100	4.7×10^{12}		59
Cs_3BiBr_6	solution/single crystal	400	0.025	0.8×10^{9}	50/60	60
$Cs_2AgBiBr_6$	solution/thin film	520	7010	5.66×10^{11}	0.956/0.995	61
$Cs_2SnCl_{6-x}Br_x$	solution/bulk crystal	590		2.71×10^{10}		62
$Cs_3Cu_2I_5$	solution/thin film	320	64.9	1.0×10^{11}	26.2/49.9	63
$Cs_2AgBiBr_6$	solution/thin film	265	1460	9.4×10^{12}	3.463/8.442	64
$Cs_3Sb_2Br_9$	solution/nanoflake	450	3800	2.6×10^{12}	48/24	43
$Cs_3Bi_2I_9$	solution/thin film	white light	7.2	1.0×10^{11}	0.247/0.23	65
Cs_2SnI_6	solution/thin film	vigible light	6	2×10^{9}		66
$Cs_3Bi_2I_9$	solution/single crystal	420	1.2	1×10^{8}		67
$Cs_3Sb_2Br_9$	solution/single crystal	480	2290	3.77×10^{12}	0.2/3.0	45
$Cs_3Bi_2I_9$	solution/nanoplate	450	33.1	1.0×10^{10}	10.2/37.2	68
$Cs_3Sb_2Br_9$	CVD/microplate	450	36.9	1.0×10^{10}	61.5/24	this work

where q is the elementary charge. Similar to the responsivity, as shown in Figure 5i, the maximum D^* of $\sim 1.0 \times 10^{10}$ Jones (cm $Hz^{1/2}$ W^{-1}) occurs at ~ 3.2 mW/cm^2, and D^* decreases and stabilizes to a value of $\sim 2.6 \times 10^9$ Jones at a high incident power of >30 mW/cm^2. The major performance parameters of our device are compared with those of previously reported lead-free all-inorganic perovskites in Table 1. The comparison in Table 1 shows that the device properties in this work are comparable to other lead-free all-inorganic perovskites. Note that the performance of our device was not measured at its optimum spectral response at an irradiation wavelength of 500 nm. Furthermore, the dark $I-V$ measurement was extended up to 10 V bias so that the trap state density (n_{trap}) in the microplate could be estimated and the results are shown in Figure S13. At a low electric field, an Ohmic region is obtained. At V_{TFL}, the current exhibits a sharp rise in the $I-V$ characteristics, indicating the transition into the trap-filled limit, where the trap states are occupied by the injected charge carriers.[58] The estimated $n_{trap} \sim 6.6 \times 10^{12}$ cm^{-3}, which demonstrates that the microplates have high quality with low defect density.

One of the major advantages of all-inorganic halide perovskites over organic hybrid materials is their material stability. The long-term stability of the $Cs_3Sb_2Br_9$ microplates and the performance of the microplate photodetector were also studied. Figure S14 compares the XRD patterns of a sample with $Cs_3Sb_2Br_9$ microplates fresh after growth with the sample after storage for 2 months in an ambient condition without any encapsulation. It is observed that after storage, the diffraction pattern is identical to the as-grown microplates, confirming that the perovskite phase is stable and there is no phase separation. However, a slight decrease in the diffraction peaks is observed. Furthermore, we measured the rocking curve of the (201) diffraction peak after 2 months storage (Figure S15). A slight increase in the FWHM ($\sim 0.055°$) is observed. This may suggest that although the $Cs_3Sb_2Br_9$ microplates show good phase and environmental stability under oxygen and moisture at room temperature, the crystallinity slightly degraded. Figure S16 shows the photoresponse curves of the $Cs_3Sb_2Br_9$ microplate photodetector as-grown and after 2 months of storage in ambient conditions, without any encapsulation. A slight degradation of $\sim 20\%$ in the photocurrent is observed, most likely related to the slight crystallinity degradation observed in the XRD measurements of the microplates. Further investigation on the correlation between material degradation and device performance under different environments is required for a detailed understanding of the degradation mechanism of this material.

CONCLUSIONS

In order to overcome the difficulties in the chemical vapor deposition of all-inorganic Pb-free $Cs_3Sb_2Br_9$ perovskites, we have developed a two-step CVD approach and successfully synthesized $Cs_3Sb_2Br_9$ perovskite microplates with a smooth hexagonal morphology, which show good crystallinity. Spectroscopic ellipsometry and photoluminescence measurements revealed that the $Cs_3Sb_2Br_9$ microplates have a band gap of ~ 2.85 eV with a large exciton binding energy of ~ 200 meV and a large Stokes shift of ~ 450 meV. Photoconductive devices fabricated using these microplates exhibit a respectable responsivity of up to 36.9 mA/W and a high detectivity, reaching 10^{10} Jones at 450 nm irradiation wavelength. Moreover, the photodetectors show stable and repeatable photoswitching characteristics with fast rise and decay times of 61.5 and 24 ms, respectively. Our results demonstrate that the 2-step CVD process is an effective approach to synthesize high-quality all-inorganic lead-free $Cs_3Sb_2Br_9$ perovskite microplates that have the potential for future high-performance optoelectronic device applications.

EXPERIMENTAL SECTION

Synthesis of $Cs_3Sb_2Br_9$ Microplates by Two-Step CVD. A two-step CVD approach was developed to grow $Cs_3Sb_2Br_9$ microplates in a home-built single-zone horizontal tube furnace (Hefei Kejing Materials Technology Co. Ltd., OTF-1200x). Prior to the growth, small pieces (20 mm × 10 mm) of glass-, sapphire-, and SiO_2-coated silicon (SiO_2/Si) substrates were cleaned ultrasonically in acetone, ethanol, and deionized water for 15 min each at room temperature. Substrates were then blown dried by nitrogen followed by heating on a hot plate at 60 °C for 30 min. Step I growth was carried out using commercial CsBr powder (99.9%, metal basis, Sigma-Aldrich) as the precursor in a boron nitride (BN) boat. The BN boat with precursors was placed at the center of the tube furnace. In order to eliminate the oxygen and moisture in the tube, the tube was evacuated to 5 mTorr and then flushed with pure Ar for 30 min and then kept at an optimized pressure of 4.5 Torr during the growth. The furnace was heated up to 530 °C for a total growth duration of 10 min. The reactant vapor was transported downstream of the quartz tube by a constant flow of high-purity argon (99.995%) at a flow rate of 50 sccm. The substrates were placed in the downstream side close to the end of the furnace, where the temperature is significantly lower than the center of the furnace. The distance between the source boat and substrate was 22 cm. After the step I growth, the furnace was cooled naturally to room temperature under a continuous Ar flow.

https://doi.org/10.1021/acsami.1c07839
ACS Appl. Mater. Interfaces 2021, 13, 35930−35940

The tube was then vented by nitrogen (N_2) gas and the boron nitride boat was taken out from the tube without disturbing the substrates. In the step II growth, $SbBr_3$ powder (98%, Sigma-Aldrich) was placed in the boron nitride boat and was introduced to the center of the furnace. Similar to the step 1 growth, the tube was again evacuated and flushed with Ar. After that the furnace was heated up to 90 °C and the $SbBr_3$ vapor was carried to the substrates with the deposition from the step I growth by a constant Ar flow at 15 sccm with the same tube pressure and holding time as in step I. After the step II growth, the furnace lid was opened immediately. Finally, to obtain $Cs_3Sb_2Br_9$ perovskite microplates, the as-grown samples were then brought back to the center of the furnace and annealed at 140 °C for 25 min with the tube backfilled with N_2 gas to atmospheric pressure. The molar ratio of CsBr and $SbBr_3$ powders used in the 2 steps was 1:10 so that microplates with stoichiometric composition can be achieved in the two steps due to the preferred evaporation of $SbBr_3$ during annealing.

Spectroscopic Ellipsometry (SE) Analysis. The SE measurements were performed using the J.A. Woollam RC2 Spectroscopic Ellipsometer system in the energy range of 0.7−6.5 eV with a rotating compensator. Measurements were performed at incident angles of 65 and 75°. The complex dielectric function of the thin-film layers was obtained by fitting the spectroscopic ellipsometry spectra (i.e., the amplitude ratio Ψ and the phase difference Δ) using a model with a three-layer structure comprising a surface roughness layer, a perovskite film layer, and the substrate. The line shape of the layer dielectric functions and the thickness of the thin-film layer were first estimated using a numerical B-spline approximation. The layer thickness is kept fixed and the dielectric function parameters were used as adjustable parameters for the fittings. Regression analysis was applied to achieve the best fitting for the experimental data. A parametric model dielectric function composed of several Tauc−Lorentz models was then used to parameterize the dielectric function similar to the procedure used in the report.[69]

Photodetector Fabrication. The photoconductive devices were fabricated on individual $Cs_3Sb_2Br_9$ perovskite microplates. $Cs_3Sb_2Br_9$ microplates were grown on an ultrasonically cleaned sapphire substrate by the two-step CVD method as outlined above. Then, Au electrodes (~40 nm thick) were deposited on the microplate by thermal evaporation using Ni grids (300 mesh) as shadow masks placed over the microplates. The electrode channel width of the device was 10 μm and the length was 73 μm. A schematic diagram of the structure of the photodetector device is shown in Figure 5a.

Characterization. Crystalline structures of the $Cs_3Sb_2Br_9$ perovskite microplate samples were determined by X-ray diffraction (XRD) using a Bruker D2 Phaser diffractometer with Cu Kα radiation (λ = 1.54184 Å). Rocking curve measurements were taken by a Rigaku SmartLab X-ray diffractometer equipped with Cu Kα radiation (λ = 1.54184 Å). Microstructural information and elemental mapping of the sample were obtained by an optical microscope (Olimpus) and a scanning electron microscope (JEOL JSM 820) equipped with energy-dispersive X-ray spectroscopy (EDX) capability. A Di MultiMode V (Veeco) AFM was used to study the morphology and dimensions of the microplates. The microplate elemental composition was also determined by X-ray flurescence (XRF) spectroscopy using a Bruker S2 Puma system equipped with a palladium (Pd) anode. Optical absorption measurements were carried out using a Perkin Elmer Lambda 2S UV−Vis spectrophotometer. Room-temperature photoluminescence spectroscopy (PL) was performed on the microplates using a home-built PL system consisting of a 320 nm cw He−Cd laser as the excitation source, a collimator, optical lens, and an ocean optics (USB 2000) spectrometer. Ultraviolet-ambient pressure photoemission spectroscopy (UV-APS) (KP technology (APS04) instrument in an N_2-filled APS module) was used to determine the valence band maximum position of the perovskite. The Ecopia HMS-5300 Hall effect measurement system was used to obtain the Hall mobility, conductivity, and carrier density of the material. The performance characteristics of the photodetectors were measured using the Agilent 4155C semiconductor analyzer in a standard probe station coupled with lasers (261, 405, 450, 532, 650 nm) as the light source. The device photoswitching response was measured by a shutter to turn the illumination on and off on the device.

■ ASSOCIATED CONTENT

Supporting Information

The Supporting Information is available free of charge at https://pubs.acs.org/doi/10.1021/acsami.1c07839.

Schematic illustration of the two-step chemical vapor deposition synthesis of $Cs_3Sb_2Br_9$ perovskite microplates; XRD patterns after each step of $Cs_3Sb_2Br_9$ perovskite microplate synthesis; XRF spectrum of as-grown sample before annealing; optical images of $Cs_3Sb_2Br_9$ microplates on different substrates; AFM images and XRF spectrum of $Cs_3Sb_2Br_9$ microplates; SEM image and EDX spectrum of a single 3D structure; ellipsometric experimental and simulated spectra of Ψ and Δ for $Cs_3Sb_2Br_9$ perovskite microplates; experimental data and modeled plot for ε_2 along with different T−L oscillators of $Cs_3Sb_2Br_9$ microplates; best fit parameters for the Tauc−Lorentz oscillators; UV−vis absorption spectrum; incident power density dependent photocurrent of the device; power-dependent photocurrent plot and the corresponding power law fitted curve; dark I−V plot of the device used to calculate trap state density; comparison of the XRD patterns of $Cs_3Sb_2Br_9$ microplates between fresh and after storage in ambient; rocking curve for (201) plane of $Cs_3Sb_2Br_9$ microplates fresh and after storage for 2 months in ambient condition; comparison of the photoresponse of the photodetector between fresh and after 2 months storage in ambient condition (PDF)

■ AUTHOR INFORMATION

Corresponding Authors

Johnny C. Ho − *Department of Materials Science and Engineering and State Key Laboratory of Terahertz and Millimeter Waves, City University of Hong Kong, Kowloon, Hong Kong SAR, China; Key Laboratory of Advanced Materials Processing & Mold (Zhengzhou University), Ministry of Education, Zhengzhou 450002, China;* orcid.org/0000-0003-3000-8794; Email: johnnyho@cityu.edu.hk

Kin Man Yu − *Department of Physics, City University of Hong Kong, Kowloon, Hong Kong SAR, China; Department of Materials Science and Engineering, City University of Hong Kong, Kowloon, Hong Kong SAR, China;* Email: kinmanyu@cityu.edu.hk

Authors

Sujit Kumer Shil − *Department of Physics, City University of Hong Kong, Kowloon, Hong Kong SAR, China; Department of Physics, Khulna University of Engineering & Technology (KUET), Khulna 9203, Bangladesh;* orcid.org/0000-0002-9114-3706

Fei Wang − *Department of Materials Science and Engineering and State Key Laboratory of Terahertz and Millimeter Waves, City University of Hong Kong, Kowloon, Hong Kong SAR, China; State Key Laboratory of Luminescence and Applications, Changchun Institute of Optics, Fine Mechanics and Physics, Chinese Academy of Sciences, Changchun 130021, China*

https://doi.org/10.1021/acsami.1c07839
ACS Appl. Mater. Interfaces 2021, 13, 35930−35940

Kingsley O. Egbo − *Department of Physics, City University of Hong Kong, Kowloon, Hong Kong SAR, China;* orcid.org/0000-0001-5303-8078

Zhengxun Lai − *Department of Materials Science and Engineering, City University of Hong Kong, Kowloon, Hong Kong SAR, China*

Ying Wang − *Department of Physics, City University of Hong Kong, Kowloon, Hong Kong SAR, China;* orcid.org/0000-0003-3643-9165

Yunpeng Wang − *State Key Laboratory of Luminescence and Applications, Changchun Institute of Optics, Fine Mechanics and Physics, Chinese Academy of Sciences, Changchun 130021, China*

Dongxu Zhao − *State Key Laboratory of Luminescence and Applications, Changchun Institute of Optics, Fine Mechanics and Physics, Chinese Academy of Sciences, Changchun 130021, China*

Sai-Wing Tsang − *Department of Materials Science and Engineering, City University of Hong Kong, Kowloon, Hong Kong SAR, China*

Complete contact information is available at: https://pubs.acs.org/10.1021/acsami.1c07839

Notes

The authors declare no competing financial interest.

■ ACKNOWLEDGMENTS

This work was financially supported by the City University of Hong Kong (Project No. 9380076), Hong Kong Scholars Program (Grant No. XJ2019027), the National Natural Science Foundation of China (Grant Nos. 11874351, 11874352, and 61805237), the General Research Fund (CityU 11306520) and the Theme-based Research (T42-103/16-N) of the Research Grants Council of Hong Kong SAR, China, and the Foshan Innovative and Entrepreneurial Research Team Program (No. 2018IT100031).

■ REFERENCES

(1) Kojima, A.; Teshima, K.; Shirai, Y.; Miyasaka, T. Organometal Halide Perovskites as Visible-Light Sensitizers for Photovoltaic Cells. *J. Am. Chem. Soc.* **2009**, *131*, 6050−6051.

(2) Saliba, M.; Matsui, T.; Domanski, K.; Seo, Ji-Y.; Ummadisingu, A.; Zakeeruddin, S. M.; Correa-Baena, J.-P.; Tress, W. R.; Abate, A.; Hagfeldt, A.; Grätzel, M. Incorporation of Rubidium Cations into Perovskite Solar Cells Improves Photovoltaic Performance. *Science* **2016**, *354*, 206−209.

(3) Liu, D.; Kelly, T. L. Perovskite Solar Cells with a Planar Heterojunction Structure Prepared Using Room-Temperature Solution Processing Techniques. *Nat. Photonics* **2014**, *8*, 133−138.

(4) Hu, X.; Zhang, X.; Liang, L.; Bao, J.; Li, S.; Yang, W.; Xie, Y. High-Performance Flexible Broadband Photodetector Based on Organolead Halide Perovskite. *Adv. Funct. Mater.* **2014**, *24*, 7373−7380.

(5) Dou, L.; Yang, Y. M.; You, J.; Hong, Z.; Chang, W. H.; Li, G.; Yang, Y. Solution-Processed Hybrid Perovskite Photodetectors with High Detectivity. *Nat. Commun.* **2014**, *5*, No. 5404.

(6) Tong, Y.; Yao, E. P.; Manzi, A.; Bladt, E.; Wang, K.; Döblinger, M.; Bals, S.; Müller-Buschbaum, P.; Urban, A. S.; Polavarapu, L.; Feldmann, J. Spontaneous Self-Assembly of Perovskite Nanocrystals into Electronically Coupled Supercrystals: Toward Filling the Green Gap. *Adv. Mater.* **2018**, *30*, No. 1801117.

(7) Pan, J.; Quan, L. N.; Zhao, Y.; Peng, W.; Murali, B.; Sarmah, S. P.; Yuan, M.; Sinatra, L.; Alyami, N. M.; Liu, J.; Yassitepe, E.; Yang, Z.; Voznyy, O.; Comin, R.; Hedhili, M. N.; Mohammed, O. F.; Lu, Z. H.; Kim, D. H.; Sargent, E. H.; Bakr, O. M. Highly Efficient Perovskite-Quantum-Dot Light-Emitting Diodes by Surface Engineering. *Adv. Mater.* **2016**, *28*, 8718−8725.

(8) Kagan, C. R.; Mitzi, D. B.; Dimitrakopoulus, C. D. Organic-Inorganic Hybrid Materials As Semiconducting Channels in Thin-Film Field-Effect Transistors. *Science* **1999**, *286*, 945−947.

(9) Zhu, L.; Zhang, H.; Lu, Q.; Wang, Y.; Deng, Z.; Hu, Y.; Lou, Z.; Cui, Q.; Hou, Y.; Teng, F. Synthesis of Ultrathin Two-Dimensional Organic-Inorganic Hybrid Perovskite Nanosheets for Polymer Field-Effect Transistors. *J. Mater. Chem. C* **2018**, *6*, 3945−3950.

(10) *Best Research-Cell Efficiency Chart*; National Renewable Energy Laboratory, 2020. https://www.nrel.gov/pv/assets/pdfs/best-research-cell-efficiencies.20200104.pdf.

(11) Ling, Y.; Yuan, Z.; Tian, Y.; Wang, X.; Wang, J. C.; Xin, Y.; Hanson, K.; Ma, B.; Gao, H. Bright Light-Emitting Diodes Based on Organometal Halide Perovskite Nanoplatelets. *Adv. Mater.* **2016**, *28*, 305−311.

(12) Luo, B.; Pu, Y. C.; Lindley, S. A.; Yang, Y.; Lu, L.; Li, Y.; Li, X.; Zhang, J. Z. Organolead Halide Perovskite Nanocrystals: Branched Capping Ligands Control Crystal Size and Stability. *Angew. Chem., Int. Ed.* **2016**, *55*, 8864−8868.

(13) Nenon, D. P.; Christians, J. A.; Wheeler, L. M.; Blackburn, J. L.; Sanehira, E. M.; Dou, B.; Olsen, M. L.; Zhu, K.; Berry, J. J.; Luther, J. M. Structural and Chemical Evolution of Methylammonium Lead Halide Perovskites during Thermal Processing from Solution. *Energy Environ. Sci.* **2016**, *9*, 2072−2082.

(14) Protesescu, L.; Yakunin, S.; Bodnarchuk, M. I.; Krieg, F.; Caputo, R.; Hendon, C. H.; Yang, R. X.; Walsh, A.; Kovalenko, M. V. Nanocrystals of Cesium Lead Halide Perovskites ($CsPbX_3$, X = Cl, Br, and I): Novel Optoelectronic Materials Showing Bright Emission with Wide Color Gamut. *Nano Lett.* **2015**, *15*, 3692−3696.

(15) Huang, Y.; Hu, Z.; Li, K.; Shao, X. First Principles Investigation on Pressure Induced Phase Transition and Photocatalytic Properties in $RbPbCl_3$. *Comput. Mater. Sci.* **2018**, *143*, 403−410.

(16) Swarnkar, A.; Marshall, A. R.; Sanehira, E. M.; Chernomordik, B. D.; Moore, D. T.; Christians, J. A.; Chakrabarti, T.; Luthe, J. M. Quantum dot-induced phase stabilization of α-$CsPbI_3$ perovskite for high-efficiency photovoltaics. *Science* **2016**, *354*, 92−96.

(17) Tong, G.; Chen, T.; Li, H.; Song, W.; Chang, Y.; Liu, J.; Yu, L.; Xu, J.; Qi, Y.; Jiang, Y. High Efficient Hole Extraction and Stable All-Bromide Inorganic Perovskite Solar Cells via Derivative-Phase Gradient Bandgap Architecture. *Sol. RRL* **2019**, *3*, No. 1900030.

(18) Liu, F.; Ding, C.; Zhang, Y.; Ripolles, T. S.; Kamisaka, T.; Toyoda, T.; Hayase, S.; Minemoto, T.; Yoshino, K.; Dai, S.; Yanagida, M.; Noguchi, H.; Shen, Q. Colloidal Synthesis of Air-Stable Alloyed $CsSn_{1-X}Pb_xI_3$ Perovskite Nanocrystals for Use in Solar Cells. *J. Am. Chem. Soc.* **2017**, *139*, 16708−16719.

(19) Dong, Y.; Gu, Y.; Zou, Y.; Song, J.; Xu, L.; Li, J.; Xue, J.; Li, X.; Zeng, H. Improving All-Inorganic Perovskite Photodetectors by Preferred Orientation and Plasmonic Effect. *Small* **2016**, *12*, 5622−5632.

(20) Shoaib, M.; Wang, X.; Zhang, X.; Wang, X.; Zhou, H.; Xu, T.; Hu, X.; Liu, H.; Fan, X.; Zheng, W.; Yang, T.; Yang, S.; Zhang, Q.; Zhu, X.; Sun, L.; Pan, A. Directional Growth of Ultralong $CsPbBr_3$ Perovskite Nanowires for High-Performance Photodetectors. *J. Am. Chem. Soc.* **2017**, *139*, 15592−15595.

(21) Zhang, Q.; Su, R.; Liu, X.; Xing, J.; Sum, T. C.; Xiong, Q. High-Quality Whispering-Gallery-Mode Lasing from Cesium Lead Halide Perovskite Nanoplatelets. *Adv. Funct. Mater.* **2016**, *26*, 6238−6245.

(22) Zhou, B.; Jiang, M.; Dong, H.; Zheng, W.; Huang, Y.; Han, J.; Pan, A.; Zhang, L. High-Temperature Upconverted Single-Mode Lasing in 3D Fully Inorganic Perovskite Microcubic Cavity. *ACS Photonics* **2019**, *6*, 793−801.

(23) Du, X.; Wu, G.; Cheng, J.; Dang, H.; Ma, K.; Zhang, Y. W.; Tan, P. F.; Chen, S. High-Quality $CsPbBr_3$ Perovskite Nanocrystals for Quantum Dot Light-Emitting Diodes. *RSC Adv.* **2017**, *7*, 10391−10396.

(24) Lin, K.; Xing, J.; Quan, L. N.; de Arquer, F. P. G.; Gong, X.; Lu, J.; Xie, L.; Zhao, W.; Zhang, D.; Yan, C.; Li, W.; Liu, X.; Lu, Y.; Kirman, J.; Sargent, E. H.; Xiong, Q.; Wei, Z. Perovskite Light-

Emitting Diodes with External Quantum Efficiency Exceeding 20 per Cent. *Nature* **2018**, *562*, 245−248.
(25) Xu, Y. F.; Yang, M. Z.; Chen, B. X.; Wang, X. D.; Chen, H. Y.; Kuang, D. B.; Su, C. Y. A $CsPbBr_3$ Perovskite Quantum Dot/Graphene Oxide Composite for Photocatalytic CO_2 Reduction. *J. Am. Chem. Soc.* **2017**, *139*, 5660−5663.
(26) Gao, G.; Xi, Q.; Zhou, H.; Zhao, Y.; Wu, C.; Wang, L.; Guo, P.; Xu, J. Novel Inorganic Perovskite Quantum Dots for Photocatalysis. *Nanoscale* **2017**, *9*, 12032−12038.
(27) De Roo, J.; Ibáñez, M.; Geiregat, P.; Nedelcu, G.; Walravens, W.; Maes, J.; Martins, J. C.; Van Driessche, I.; Kovalenko, M. V.; Hens, Z. Highly Dynamic Ligand Binding and Light Absorption Coefficient of Cesium Lead Bromide Perovskite Nanocrystals. *ACS Nano* **2016**, *10*, 2071−2081.
(28) Yettapu, G. R.; Talukdar, D.; Sarkar, S.; Swarnkar, A.; Nag, A.; Ghosh, P.; Mandal, P. Terahertz Conductivity within Colloidal $CsPbBr_3$ Perovskite Nanocrystals: Remarkably High Carrier Mobilities and Large Diffusion Lengths. *Nano Lett.* **2016**, *16*, 4838−4848.
(29) Sun, S.; Yuan, D.; Xu, Y.; Wang, A.; Deng, Z. Ligand-Mediated Synthesis of Shape-Controlled Cesium Lead Halide Perovskite Nanocrystals via Reprecipitation Process at Room Temperature. *ACS Nano* **2016**, *10*, 3648−3657.
(30) Shi, D.; Adinolfi, V.; Comin, R.; Yuan, M.; Alarousu, E.; Buin, A.; Chen, Y.; Hoogland, S.; Rothenberger, A.; Katsiev, K.; Losovyj, Y. B.; Zhang, X.; Dowben, P. A.; Mohammed, O. F.; Sargent, E. H.; Bakr, O. M. Low Trap-State Density and Long Carrier Diffusion in Organolead Trihalide Perovskite Single Crystals. *Science* **2015**, *347*, 519−522.
(31) Yang, Y.; Yan, Y.; Yang, M.; Choi, S.; Zhu, K.; Luther, J. M.; Beard, M. C. Low Surface Recombination Velocity in Solution-Grown $CH_3NH_3PbBr_3$ Perovskite Single Crystal. *Nat. Commun.* **2015**, *6*, No. 7961.
(32) Chen, J.; Luo, Z.; Fu, Y.; Wang, X.; Czech, K. J.; Shen, S.; Guo, L.; Wright, J. C.; Pan, A.; Jin, S. Tin(IV)-Tolerant Vapor-Phase Growth and Photophysical Properties of Aligned Cesium Tin Halide Perovskite ($CsSnX_3$; X = Br, I) Nanowires. *ACS Energy Lett.* **2019**, *4*, 1045−1052.
(33) Jellicoe, T. C.; Richter, J. M.; Glass, H. F. J.; Tabachnyk, M.; Brady, R.; Dutton, S. E.; Rao, A.; Friend, R. H.; Credgington, D.; Greenham, N. C.; Böhm, M. L. Synthesis and Optical Properties of Lead-Free Cesium Tin Halide Perovskite Nanocrystals. *J. Am. Chem. Soc.* **2016**, *138*, 2941−2944.
(34) Hoefler, S. F.; Trimmel, G.; Rath, T. Progress on Lead-Free Metal Halide Perovskites for Photovoltaic Applications: A Review. *Monatsh. Chem.* **2017**, *148*, 795−826.
(35) Wang, A.; Guo, Y.; Muhammad, F.; Deng, Z. Controlled Synthesis of Lead-Free Cesium Tin Halide Perovskite Cubic Nanocages with High Stability. *Chem. Mater.* **2017**, *29*, 6493−6501.
(36) Wu, X.; Song, W.; Li, Q.; Zhao, X.; He, D.; Quan, Z. Synthesis of Lead-Free $CsGeI_3$ Perovskite Colloidal Nanocrystals and Electron Beam-Induced Transformations. *Chem. - Asian J.* **2018**, *13*, 1654−1659.
(37) Singh, A.; Boopathi, K. M.; Mohapatra, A.; Chen, Y. F.; Li, G.; Chu, C. W. Photovoltaic Performance of Vapor-Assisted Solution-Processed Layer Polymorph of $Cs_3Sb_2I_9$. *ACS Appl. Mater. Interfaces* **2018**, *10*, 2566−2573.
(38) Umar, F.; Zhang, J.; Jin, Z.; Muhammad, I.; Yang, X.; Deng, H.; Jahangeer, K.; Hu, Q.; Song, H.; Tang, J. Dimensionality Controlling of $Cs_3Sb_2I_9$ for Efficient All-Inorganic Planar Thin Film Solar Cells by HCl-Assisted Solution Method. *Adv. Opt. Mater.* **2019**, *7*, No. 1801368.
(39) Ghosh, B.; Chakraborty, S.; Wei, H.; Guet, C.; Li, S.; Mhaisalkar, S.; Mathews, N. Poor Photovoltaic Performance of $Cs_3Bi_2I_9$: An Insight through First-Principles Calculations. *J. Phys. Chem. C* **2017**, *121*, 17062−17067.
(40) Zhang, Y.; Yin, J.; Parida, M. R.; Ahmed, G. H.; Pan, J.; Bakr, O. M.; Brédas, J. L.; Mohammed, O. F. Direct-Indirect Nature of the Bandgap in Lead-Free Perovskite Nanocrystals. *J. Phys. Chem. Lett.* **2017**, *8*, 3173−3177.
(41) Saparov, B.; Hong, F.; Sun, J. P.; Duan, H. S.; Meng, W.; Cameron, S.; Hill, I. G.; Yan, Y.; Mitzi, D. B. Thin-Film Preparation and Characterization of $Cs_3Sb_2I_9$: A Lead-Free Layered Perovskite Semiconductor. *Chem. Mater.* **2015**, *27*, 5622−5632.
(42) Lu, C.; Itanze, D. S.; Aragon, A. G.; Ma, X.; Li, H.; Ucer, K. B.; Hewitt, C.; Carroll, D. L.; Williams, R. T.; Qiu, Y.; Geyer, S. M. Synthesis of Lead-Free $Cs_3Sb_2Br_9$ Perovskite Alternative Nanocrystals with Enhanced Photocatalytic CO2 Reduction Activity. *Nanoscale* **2020**, *12*, 2987−2991.
(43) Zheng, Z.; Hu, Q.; Zhou, H.; Luo, P.; Nie, A.; Zhu, H.; Gan, L.; Zhuge, F.; Ma, Y.; Song, H.; Zhai, T. Submillimeter and Lead-Free $Cs_3Sb_2Br_9$ Perovskite Nanoflakes: Inverse Temperature Crystallization Growth and Application for Ultrasensitive Photodetectors. *Nanoscale Horiz.* **2019**, *4*, 1372−1379.
(44) Ma, Z.; Shi, Z.; Yang, D.; Zhang, F.; Li, S.; Wang, L.; Wu, D.; Zhang, Y.; Na, G.; Zhang, L.; Li, X.; Zhang, Y.; Shan, C. Electrically-Driven Violet Light-Emitting Devices Based on Highly Stable Lead-Free Perovskite $Cs_3Sb_2Br_9$ Quantum Dots. *ACS Energy Lett.* **2020**, 385−394.
(45) Liu, P.; Liu, Y.; Zhang, S.; Li, J.; Wang, C.; Zhao, C.; Nie, P.; Dong, Y.; Zhang, X.; Zhao, S.; Wei, G. Lead-Free $Cs_3Sb_2Br_9$ Single Crystals for High Performance Narrowband Photodetector. *Adv. Opt. Mater.* **2020**, No. 2001072.
(46) Pan, D.; Fu, Y.; Chen, J.; Czech, K. J.; Wright, J. C.; Jin, S. Visualization and Studies of Ion-Diffusion Kinetics in Cesium Lead Bromide Perovskite Nanowires. *Nano Lett.* **2018**, *18*, 1807−1813.
(47) Hossain, M. K.; Guo, P.; Qarony, W.; Tsang, Y. H.; Liu, C.; Tsang, S. W.; Ho, J. C.; Yu, K. M. Controllable Optical Emission Wavelength in All-Inorganic Halide Perovskite Alloy Microplates Grown by Two-Step Chemical Vapor Deposition. *Nano Res.* **2020**, *13*, 2939−2949.
(48) Kristin, P. Materials Data on $Cs_3Sb_2Br_9$ (SG:164) by Materials Project, 2014. DOI: 10.17188/1276711.
(49) Ruf, F.; Aygüler, M. F.; Giesbrecht, N.; Rendenbach, B.; Magin, A.; Docampo, P.; Kalt, H.; Hetterich, M. Temperature-Dependent Studies of Exciton Binding Energy and Phase-Transition Suppression in $(Cs,FA,MA)Pb(I,Br)_3$ Perovskites. *APL Mater.* **2019**, *7*, No. 031113.
(50) Yang, B.; Yin, L.; Niu, G.; Yuan, J. H.; Xue, K. H.; Tan, Z.; Miao, X. S.; Niu, M.; Du, X.; Song, H.; Lifshitz, E.; Tang, J. Lead-Free Halide Rb_2CuBr_3 as Sensitive X-Ray Scintillator. *Adv. Mater.* **2019**, *31*, No. 1904711.
(51) Dammak, H.; Yangui, A.; Triki, S.; Abid, Y.; Feki, H. Structural Characterization, Vibrational, Optical Properties and DFT Investigation of a New Luminescent Organic-Inorganic Material: $(C_6H_{14}N)_3Bi_2I_9$. *J. Lumin.* **2015**, *161*, 214−220.
(52) Swarnkar, A.; Chulliyil, R.; Ravi, V. K.; Irfanullah, M.; Chowdhury, A.; Nag, A. Colloidal $CsPbBr_3$ Perovskite Nanocrystals: Luminescence beyond Traditional Quantum Dots. *Angew. Chem., Int. Ed.* **2015**, *54*, 15424−15428.
(53) Shil, S. K.; Wang, F.; Lai, Z.; Meng, Y.; Wang, Y.; Zhao, D.; Hossain, M. K.; Egbo, K. O.; Wang, Y.; Yu, K. M.; Ho, J. C. Crystalline All-Inorganic Lead-Free $Cs_3Sb_2I_9$ Perovskite Microplates with Ultra-Fast Photoconductive Response and Robust Thermal Stability *Nano Res.* 2021, *121*. DOI: 10.1007/s12274-021-3351-x.
(54) Pal, J.; Manna, S.; Mondal, A.; Das, S.; Adarsh, K. V.; Nag, A. Colloidal Synthesis and Photophysics of $M_3Sb_2I_9$ (M = Cs and Rb) Nanocrystals: Lead-Free Perovskites. *Angew. Chem., Int. Ed.* **2017**, *56*, 14187−14191.
(55) Kind, H.; Yan, H.; Messer, B.; Law, M.; Yang, P. Nanowire Ultraviolet Photodetectors and Optical Switches. *Adv. Mater.* **2002**, *14*, 158−160.
(56) Gong, M.; Sakidja, R.; Goul, R.; Ewing, D.; Casper, M.; Stramel, A.; Elliot, A.; Wu, J. Z. High-Performance All-Inorganic $CsPbCl_3$ Perovskite Nanocrystal Photodetectors with Superior Stability. *ACS Nano* **2019**, *13*, 1772−1783.
(57) Konstantatos, G.; Clifford, J.; Levina, L.; Sargent, E. H. Sensitive Solution-Processed Visible-Wavelength Photodetectors. *Nat. Photonics* **2007**, *1*, 531−534.

(58) Liu, Y.; Zhang, Y.; Yang, Z.; Yang, D.; Ren, X.; Pang, L.; Liu, S. F. Thinness- and Shape-Controlled Growth for Ultrathin Single-Crystalline Perovskite Wafers for Mass Production of Superior Photoelectronic Devices. *Adv. Mater.* **2016**, *28*, 9204−9209.
(59) Zhang, Y.; Liu, Y.; Xu, Z.; Ye, H.; Yang, Z.; You, J.; Liu, M.; He, Y.; Kanatzidis, M. G.; Liu, S. F. Nucleation-Controlled Growth of Superior Lead-Free Perovskite $Cs_3Bi_2I_9$ Single-Crystals for High-Performance X-Ray Detection. *Nat. Commun.* **2020**, *11*, No. 6428.
(60) Tang, Y.; Liang, M.; Chang, B.; Sun, H.; Zheng, K.; Pullerits, T.; Chi, Q. Lead-Free Double Halide Perovskite Cs_3BiBr_6 with Well-Defined Crystal Structure and High Thermal Stability for Optoelectronics. *J. Mater. Chem. C* **2019**, *7*, 3369−3374.
(61) Lei, L. Z.; Shi, Z. F.; Li, Y.; Ma, Z. Z.; Zhang, F.; Xu, T. T.; Tian, Y. T.; Wu, D.; Li, X. J.; Du, G. T. High-Efficiency and Air-Stable Photodetectors Based on Lead-Free Double Perovskite $Cs_2AgBiBr_6$ Thin Films. *J. Mater. Chem. C* **2018**, *6*, 7982−7988.
(62) Zhou, J.; Luo, J.; Rong, X.; Wei, P.; Molokeev, M. S.; Huang, Y.; Zhao, J.; Liu, Q.; Zhang, X.; Tang, J.; Xia, Z. Lead-Free Perovskite Derivative $Cs_2SnCl_{6-x}Br_x$ Single Crystals for Narrowband Photodetectors. *Adv. Opt. Mater.* **2019**, *7*, No. 1900139.
(63) Zhang, Z. X.; Li, C.; Lu, Y.; Tong, X. W.; Liang, F. X.; Zhao, X. Y.; Wu, D.; Xie, C.; Luo, L. B. Sensitive Deep Ultraviolet Photodetector and Image Sensor Composed of Inorganic Lead-Free $Cs_3Cu_2I_5$ Perovskite with Wide Bandgap. *J. Phys. Chem. Lett.* **2019**, *10*, 5343−5350.
(64) Li, Y.; Shi, Z.; Lei, L.; Li, S.; Yang, D.; Wu, D.; Xu, T.; Tian, Y.; Lu, Y.; Wang, Y.; Zhang, L.; Li, X.; Zhang, Y.; Du, G.; Shan, C. Ultrastable Lead-Free Double Perovskite Photodetectors with Imaging Capability. *Adv. Mater. Interfaces* **2019**, *6*, No. 1900188.
(65) Li, W. G.; Wang, X. D.; Liao, J. F.; Jiang, Y.; Kuang, D. B. Enhanced On−Off Ratio Photodetectors Based on Lead-Free $Cs_3Bi_2I_9$ Single Crystal Thin Films. *Adv. Funct. Mater.* **2020**, *30*, No. 1909701.
(66) Krishnaiah, M.; Khan, M. M. I.; Kumar, A.; Jin, S. H. Impact of CsI Concentration, Relative Humidity, and Annealing Temperature on Lead-Free Cs2SnI6 Perovskites: Toward Visible Light Photodetectors Application. *Mater. Lett.* **2020**, *269*, No. 127675.
(67) Zhang, H.; Xu, Y.; Sun, Q.; Dong, J.; Lu, Y.; Zhang, B.; Jie, W. Lead Free Halide Perovskite $Cs_3Bi_2I_9$ Bulk Crystals Grown by a Low Temperature Solution Method. *CrystEngComm* **2018**, *20*, 4935−4941.
(68) Qi, Z.; Fu, X.; Yang, T.; Li, D.; Fan, P.; Li, H.; Jiang, F.; Li, L.; Luo, Z.; Zhuang, X.; Pan, A. Highly Stable Lead-Free $Cs_3Bi_2I_9$ Perovskite Nanoplates for Photodetection Applications. *Nano Res.* **2019**, *12*, 1894−1899.
(69) Egbo, K. O.; Liu, C. P.; Hossain, M. K.; Ho, C. Y.; Kwok, C. G.; Shil, S. K.; Ezeh, C. V.; Wang, Y.; Yu, K. M. Controlling the P-Type Conductivity and Composition Range for Bipolar Conduction in $Ni_XCd_{1-X}O$ Alloys by Acceptor Doping. *J. Phys. Chem. C* **2020**, *124*, 20000−20009.

https://doi.org/10.1021/acsami.1c07839
ACS Appl. Mater. Interfaces 2021, 13, 35930−35940